

RESEARCH ARTICLE | MARCH 01 2024

Deep learning-based data processing method for transient thermoreflectance measurements

Special Collection: [Machine Learning for Thermal Transport](#)

Yali Mao  ; Shaojie Zhou  ; Weiyuan Tang  ; Mei Wu; Haochen Zhang  ; Haiding Sun  ;
Chao Yuan  



J. Appl. Phys. 135, 095102 (2024)

<https://doi.org/10.1063/5.0192164>



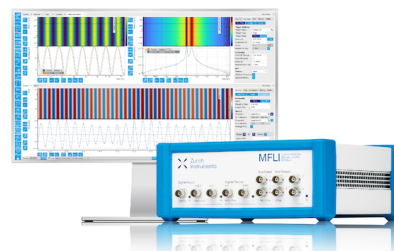
Challenge us.

What are your needs for periodic
signal detection?



Zurich
Instruments

[Find out more](#)



Deep learning-based data processing method for transient thermoreflectance measurements

Cite as: J. Appl. Phys. 135, 095102 (2024); doi: 10.1063/5.0192164

Submitted: 18 December 2023 · Accepted: 14 February 2024 ·

Published Online: 1 March 2024



Yali Mao,¹ Shaojie Zhou,¹ Weiyuan Tang,² Mei Wu,³ Haochen Zhang,⁴ Haiding Sun,⁴
and Chao Yuan^{1,a)}

AFFILIATIONS

¹The Institute of Technological Sciences, Wuhan University, Wuhan 430072, China

²School of Power and Mechanical Engineering, Wuhan University, Wuhan 430072, China

³State Key Discipline Laboratory of Wide Band-Gap Semiconductor Technology, School of Microelectronics, Xidian University, Xi'an 710071, China

⁴GaN Laboratory, School of Microelectronics, University of Science and Technology of China, Anhui 230026, China

Note: This paper is part of the special topic, Machine Learning for Thermal Transport.

a) Author to whom correspondence should be addressed: chaoyuan@whu.edu.cn

ABSTRACT

Pump-probe thermoreflectance has been commonly applied for characterizing the thermal properties of materials. Generally, a reliable and efficient non-linear fitting process is often implemented to extract unknown thermal parameters during the pump-probe thermoreflectance characterizations. However, when it comes to processing large amounts of data acquired from similar structural samples, non-linear fitting process appears to be very time-consuming and labor-intensive to search for the best fitting for every testing curve. Herein, we propose to apply deep learning (DL) approach to nanosecond transient thermoreflectance technique for high-throughput experimental data processing. We first investigated the effect of training set parameters (density and bounds) on the predictive performance of the DL model, providing a guidance to optimize the DL model. Then, the DL model is further verified in the measurement of the bulk sapphire, SiC, diamond samples, and GaN-based multilayer structures, demonstrating its capability of analyzing the results with high accuracy. Compared to the conventional non-linear fitting method (such as Global Optimization), the computation time of the new model is 1000 times lower. Such a data-driven DL model enables the faster inference and stronger fitting capabilities and is particularly efficient and effective in processing data acquired from wafer-level measurements with similar material structures.

© 2024 Author(s). All article content, except where otherwise noted, is licensed under a Creative Commons Attribution (CC BY) license (<http://creativecommons.org/licenses/by/4.0/>). <https://doi.org/10.1063/5.0192164>

I. INTRODUCTION

Pump-probe thermoreflectances, such as time-domain thermoreflectance (TDTR),^{1–3} frequency-domain thermoreflectance (FDTR),^{4,5} transient thermoreflectance (TTR),^{6–10} and steady-state thermoreflectance (SSTR)^{11,12}, have been regarded as the robust techniques for characterizing the thermal transport properties (e.g., thermal conductivity, thermal boundary conductance, etc.) of both bulk materials and multilayer thin films. The traditional way of analyzing pump-probe thermoreflectance data is to combine the heat transfer model with a fitting algorithm^{6,7,13–15} to infer the thermal transport properties from the measured reflectance/

temperature response. The fitting algorithm is used to find the optimal solution for thermal transport properties that make the thermal model curves coincide with the tested curves. Such fitting algorithms are typically based on non-linear least squares fitting methods, including the Global Optimization, Levenberg–Marquart, Trust Region, Simulated Annealing, Genetic Algorithm, etc. In fact, these non-linear fitting processes are quite reliable and have been used for a long time in the pump-probe thermoreflectance characterizations. As pump-probe thermoreflectance becomes a widely used method in various application (e.g., power and radio-frequency electronics, thermoelectrics, ceramics materials in aerospace), there is a tendency to apply it as a process monitoring tool

29 October 2024 18:18:32

in a manufacturing line.¹⁶ As a result, the capability of large-batch wafer-level testing is highly demanded for the thermoreflectance techniques. With such demand, non-linear fitting process in the thermoreflectance measurement, while already efficient, is sometimes labor-intensive and time-consuming. Because, it requires laborious tuning of fitting parameters until thermal model curves coincide with the measured curves case by case. Therefore, a more efficient high-throughput data analysis method is highly in demand.

Deep learning (DL) technique has the ability to make rapid and effective predictions and is particularly suitable for efficient and high-throughput experimental data processing.¹⁷ It would be very feasible to process large volumes of data in pump-probe thermoreflectance characterizations with the deep learning technique. For the traditional FDTR and TDTR methods, DL techniques have been applied to process the measurement data.^{18,19} Large data sets are generated by inputting different combinations of parameters into the thermal model. By learning the large amount of data, the DL model is able to quickly identify features of the data, building intelligent connections between features and output properties. The unknown thermal parameters can be predicted after inputting the experimental data into the DL model. Nanosecond-based transient thermoreflectance (TTR) is a recently developed new form of the pump-probe thermoreflectance method that has also been often used for characterizing the thermal properties of materials.^{6–10} The difference between TTR and TDTR/FDTR differences lie in the characteristics of pump and probe lasers (e.g., wavelength, pulsed or continuous-wave, pulse width, etc.) as well as the arrangements of optic, mechanical, and electrical components. The analytical heat transfer model of TTR is also different to the other techniques. Investigating the feasibility of applying deep learning to TTR is of great interest. In addition, the prediction capability of the DL model is dependent on the quality of training set, which is determined based on the material structures and properties. The structures and properties of materials to be characterized could be vastly different. However, the way of effectively building reliable training set for various different materials has not yet been clarified in the previous machine/deep learning-based FDTR and TDTR.^{4,18}

In this paper, we propose to apply DL method to processing the data acquired from TTR. Further, the effect of the parameters (density and bounds) of the training set on the predictive performance of the DL model is studied in depth, figuring out a reliable method of building training sets. Furthermore, we confirm our DL models using the samples with different structures and properties to illustrate the potential of DL models for effectively and efficiently analyzing complex structural samples during the TTR data analysis.

II. MULTIPLE PROBE WAVELENGTHS TRANSIENT THERMOTRANSFER (TTR) METHOD

The multiple probe wavelengths TTR (MW-TTR) is applied in this study. The idea of MW-TTR is to utilize a low-repetition rate nanosecond laser as the pump beam to heat the sample surface and multiple continuous wavelength (CW) lasers as the probes to

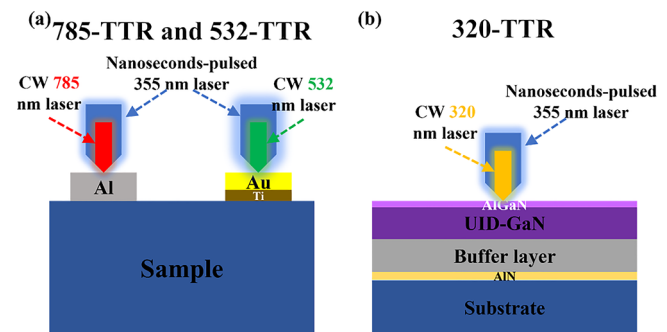


FIG. 1. (a) Schematic of the 532-TTR and 785-TTR measurement configurations. (b) Schematic of the 320-TTR for GaN-based epitaxial wafer.

monitor the surface $\Delta R/R$ as a result of the surface ΔT at different surfaces.⁶ A 10.8 kHz, 3.2 ns, and 355 nm pulsed laser is applied as the pump. Three different wavelengths' CW lasers are applied as the probe, i.e., 532, 785, and 320 nm, respectively. As shown in Fig. 1(a), the TTR technique with the 532 or 785 nm probe beam (referred to as the 532-TTR and 785-TTR, respectively) is the conventional metal transducer TTR, where a metal layer (gold or aluminum) is required to be deposited on the sample surface as the measurement transducer.^{20,21} The technique with the 320 nm probe beam (referred to as 320-TTR) has been developed for the transducer-less characterization of GaN-based epitaxial wafers.^{22,23} As schematically shown in Fig. 1(b), the 320-TTR measurement is conducted directly on the surface of GaN-based epitaxial wafer without the need of metal transducer. Despite the difference in probe beams, the other components such as the photodetector and the oscilloscope are the same in the three TTRs. The thermoreflectance transient signals (either measured from 532, 785, or 320 nm) are received by a silicon amplified photodetector with a bandwidth of 400 MHz (<1 ns rise time). Then, a digital oscilloscope with a bandwidth (500 MHz) receives the signals from the photodetector. A Keplerian beam expander was placed in the pump beam route to adjust the pump spot size continuously. We adjusted the beam expander to ensure a similar pump spot size for the three TTRs. The spot sizes of the pump and probe beams for each system (i.e., 532-TTR, 785-TTR, and 320-TTR) were measured by a beam profiler (BP209-VIS, Thorlabs). The $1/e^2$ radius of the Gaussian probe beam for 532, 785, and 320 nm were 3.5, 8.7, and $17\ \mu\text{m}$, respectively. The $1/e^2$ radius of the Gaussian pump beam was 62, 65, and $62\ \mu\text{m}$, respectively. It is worth stating that the $1/e^2$ diameter of the pump beam is around $120\ \mu\text{m}$, which is much larger than the thermal penetration depth ($d_p = \sqrt{2Kt/(\rho C)}$, K is the thermal conductivity, ρ the density, C the specific heat capacity, and t the measurement time window). Therefore, this work only considers the cross-plane thermal properties.

The TTR heat transfer analytical model⁶ is used to generate data for deep learning. The model considers photothermal pulse-induced heat conduction in a N -layer medium, calculating the response of the surface temperature as a function of time. The analytical equation for the surface temperature rise,

29 October 2024 18:18:32

$$\Delta T(t) = \frac{A_{abs}}{2\pi j} \int_{\sigma-j\infty}^{\sigma+j\infty} \exp(st) ds \left(\int_0^\infty \frac{1}{4\pi} \exp\left(-\frac{\omega_0^2 \beta^2}{8}\right) * \exp\left(\frac{s(st_0^2 - 2t_m)}{2}\right) \operatorname{erfc}\left(\frac{st_0 - t_m}{\sqrt{2}}\right) \widehat{Z}_n \beta J_0(\beta r) d\beta \right), \quad (1)$$

$$\widehat{Z}_n = Z_n \frac{\widehat{Z}_{n-1} + Z_n \tan h(\gamma_n d_n)}{Z_n + \widehat{Z}_{n-1} \tan h(\gamma_n d_n)}, \quad (2)$$

where

$$Z_i = \begin{cases} \infty & i = 1, \text{ adiabatic condition at n-layer bottom,} \\ \frac{1}{k_i \gamma_i}, & i > 1, \end{cases} \quad (3)$$

$$\gamma_i = \sqrt{\frac{\rho_i c_i}{k_{z,i}} s + \frac{k_{r,i}}{k_{z,i}} \beta^2}. \quad (4)$$

Here, A_{abs} is the absorbed laser energy, t is the time, ω_0 is the $1/e^2$ radius of pump laser on the sample surface, $t_0 = h/(2\sqrt{2\ln 2})$, h is the FWHM pulse width, t_m is the time of pulse reaching maximum, \widehat{Z}_n is the thermal impedance of the stack of materials, $J_0(\beta r)$ is the first kind Bessel function, $k_{z,i}$ is the cross-plane thermal conductivity of i th layer, $k_{r,i}$ is the in-plane thermal conductivity of i th layer, ρ_i is the density of i th layer, c_i is the specific heat capacity of i th layer, and (β, s) is the spatial and temporal frequency domain. The more detailed description and explanation can be found in Ref. 6. After obtaining $\Delta T(t)$, $\Delta T(t)$ is normalized by its maximum, i.e., $\Delta T(t)/\text{Max}[\Delta T(t)]$. This is because the

normalized temperature rise ($\Delta T(t)/\text{Max}[\Delta T(t)]$) is used in the TTR data analysis.^{6,7,22}

III. DEEP LEARNING (DL) MODEL

Figure 2 shows the outline of the Deep Learning (DL) method. First, a TTR data set was obtained based on the existed TTR heat transfer analytical model,⁶ which was described in Sec. II. The temperature response contains the information of the physical properties (thermal conductivity, thermal boundary conductance, specific heat capacity, density, and thickness) of the N-layer medium and the laser parameters (pump laser pulse width, pump laser spot size, and probe laser spot size). Typically, thermal conductivity of all layers excluding the metal transducer (k_i) and the thermal boundary conductance between any adjacent layers (TBC_{i-i+1}) are the unknown parameters, and all the other parameters are treated as the controlled parameters. The controlled parameters are normally obtained by the separate measurements or the literature.

Building the training sets needs determine the upper and lower bounds of unknown parameters and the density of training set. For the unknown parameters (such as, k_i and TBC_{i-i+1}), the upper and lower bounds can be determined based on literature reported values by experiments and predictive models, for example, thermal conductivity calculation based on Density Functional Theory (DFT)^{24,25} or Callaway model^{26,27} and TBC calculation

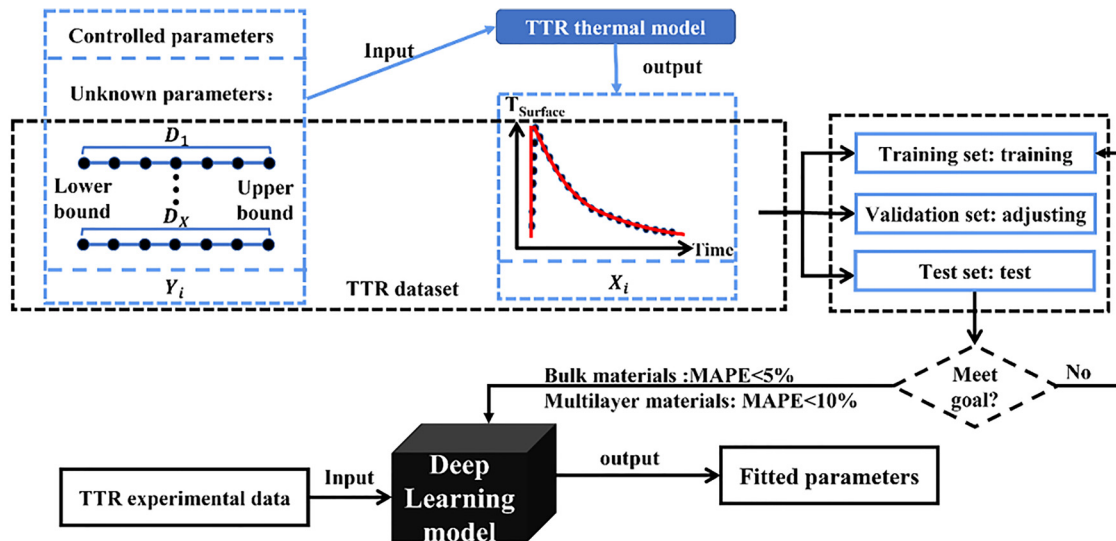


FIG. 2. Schematic diagram of the processes applying a DL model for data processing in TTR experiments.

based on Diffusion Mismatch Model (DMM).^{28,29} A series of values are assigned for the unknown parameters. These values are selected uniformly spaced within the upper and lower bounds of unknown parameters. We define the number of selected values as the training set density (D). The interval between values changes with D and is equal to (upper bound-lower bound)/(D-1). All combinations of selected values of unknown parameters (i.e., k_i and TBC_{i-i+1}), as well as the controlled parameters, are input into the TTR thermal transfer model, which outputs the TTR transients (reflectance change as function of time). All the select values of unknown parameters and the corresponding TTR transients consist of the TTR data set. The size of the data set is equal to the $D_1 \times D_2 \times \dots \times D_X$, X is the number of unknown parameters. The data set is divided into a training set, a validation set, and a test set with the ratio of 0.85:0.1:0.05. The training set is used to train the DL model, the validation set is used to adjust the hyperparameters of the model, and the test set is used to evaluate the accuracy of the trained model.

The deep learning model is built and trained using pytorch. The inputs are first batch normalized (BN) and then transformed to a fully connected (FC) layer. The inputs consist of TTR transients in the data set. The first FC layer has an output size of 100 and uses the hyperbolic tangent (tanh) activation function. The output of the first FC layer is then batch normalized (BN). The second FC layer has an output size of 50 and uses the hyperbolic tangent (tanh) activation function. The output of the second FC layer is then batch normalized (BN). The third FC layer has an output size of 10 and uses the ReLU activation function. The number of unknown thermal properties determines the size of the last FC layer. The last FC layer uses the ReLU activation and outputs the value as the final prediction. The FC layer is the main layer. It connects each neuron to all neurons in the previous layer, making it possible to capture complex non-linear relationships and regresses inputs efficiently. The activation function introduces non-linearity into the output of FC, making it possible to learn complex information. The training process uses mean square error (MSE) as the loss function. We choose the mean absolute percentage error (MAPE) to assess the performance of the trained DL model,

$$MSE = \frac{1}{m} \sum_{i=1}^m (f(X_i) - Y_i)^2, \quad (5)$$

$$MAPE = \frac{1}{n} \sum_{i=1}^n \frac{|f(X_i) - Y_i|}{Y_i}. \quad (6)$$

Here, f is the output of the candidate DL model, i.e., the prediction of unknown parameters, Y_i is the selected values for the unknown parameters and X_i is the corresponding TTR signal, m is the number of training set, and n is the number of test set. If the MAPE fail to meet the target (for the bulk materials, $MAPE < 5\%$; for multilayer materials, $MAPE < 10\%$), the parameters of the DL algorithm will be slightly tuned by adjusting the hyperparameters, and another cycle of the training and evaluation process will be performed. Normally, generating an ideal DL model requires iterative training, evaluation, and parameter tuning. The tuning of the hyperparameters is determined through grid-search cross-validation implemented in Skit-learn, where all possible combinations are validated by their performance on the validation set.³⁰ Finally, the experimental data are input to the ideal deep learning model to predict unknown parameters. The whole calculation is based on python by a desktop computer with 8-core 3.6 GHz processors.

IV. RESULTS AND DISCUSSION

In this section, we first discuss the effect of training set on DL model's predicting capability with virtual materials and propose the guide for building the training set. Then, the model's fitting capability is evaluated with the experimental results.

A. Effect of training set's density (D)

We constructed the virtual Al coated sapphire (Al-Sa), Au coated SiC (Au-SiC), and Au coated diamond (Au-diamond) materials. The details of the virtual material information are given in Table I. The 785-TTR and 532-TTR system parameters were described in Sec. II. The thermal conductivity (TC) and thermal boundary conductance between the metal and the substrate (TBC) of these materials are treated as the unknown parameters to be fitted. According to the literature^{3,38-49} and large amount of measurement data from our own lab, the lower and upper bounds of the k and TBC are assumed, with the details given in Table I. In order to discuss the effect of training set's density (D) on the DL model, we constructed a series of training sets with the D ranging

TABLE I. Materials' thickness, density, specific heat capacity, and thermal conductivity information at room temperature and unknown parameters' bounds.

	Thickness (nm)	Density (kg/m ³)	Specific heat capacity (J/kg K)	Thermal conductivity (W/m K)	Lower bounds	Upper bounds
Au	100	19 300 ³¹	129 ³²	120
Al	80	2 700 ³¹	897 ³³	120
Sa	1 000 000	3 980 ³⁴	778 ³⁵	Fit	20	50
SiC	1 000 000	3 260 ³¹	690 ³⁶	Fit	250	500
Diamond	1 000 000	3 150 ³⁷	500 ³⁷	Fit	100	2 000
TBC _{Al/Sa} (MW/m ² K)		Fit			20	300
TBC _{Au/SiC} (MW/m ² K)		Fit			20	300
TBC _{Au/Diamond} (MW/m ² K)		Fit			20	400

29 October 2024 18:18:32

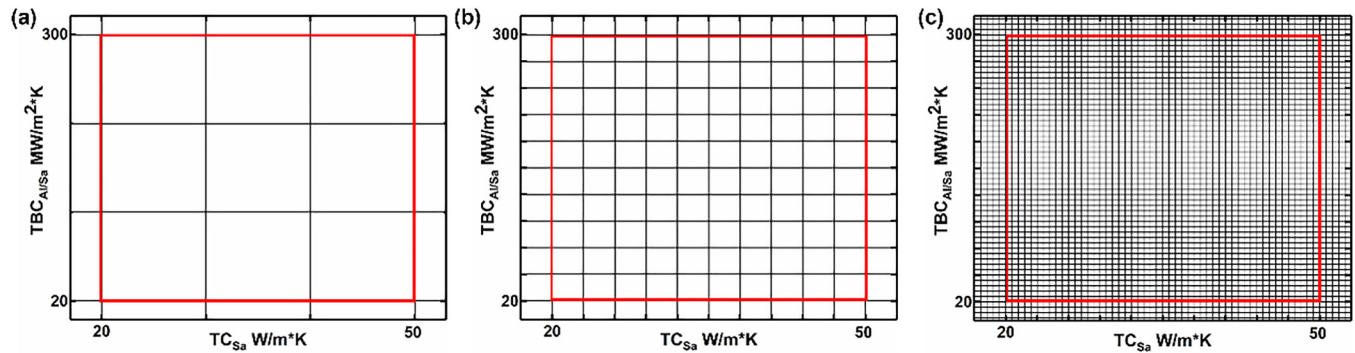


FIG. 3. Schematic diagram of training set densities (D): (a) 3, (b) 10, and (c) 50.

from 3 to 100 to train the DL model. There are D discrete values chosen uniformly spaced within the bounds of unknown parameters. For instance, if D is equal to 10, there will be 10×10 combinations of TC and TBC as the TTR thermal model inputs. Figure 3 shows the details of training set diagrams for the virtual Al-Sa.

With the TTR model, we created the testing curves for virtual Al-Sa by assuming the TC and TBC to be 35 W/mK and 180 MW/m² K, respectively, and for virtual Au-SiC with the TC and TBC to be 350 W/mK and 160 MW/m² K, respectively, and for virtual Au-diamond with the TC and TBC to be 1200 W/mK and 140 MW/m² K, respectively. We then used the DL model trained from various D to output the TBC and TC from the testing curves. The fitted $TBC_{Al/Sa}$ and TC_{Sa} as a function of D and pitch are plotted in Figs. 4(a) and 4(b), respectively. As shown in Fig. 4(a), $TBC_{Al/Sa}$ oscillates at $D < 12$, whereas at $D > 12$, the $TBC_{Al/Sa}$ stabilizes with an error of no more than $\pm 5\%$. As shown in Fig. 4(b), TC_{Sa} shows the trend that is similar to $TBC_{Al/Sa}$. TC_{Sa} tends to stabilize after $D > 15$. For the Au-SiC material, both TC_{SiC} and $TBC_{Au/SiC}$ stabilize at $D \sim 20$ as seen in Figs. 4(c) and 4(d), and for the Au-diamond material, both $TC_{Diamond}$ and $TBC_{Au/Diamond}$ stabilizes at $D \sim 15$ as shown in Figs. 4(e) and 4(f). As a result, the size of the training set density affects the performance of the algorithm and the accuracy of the model. We investigated this effect using different metal-bulk materials (Al-Sa, Au-SiC, and Au-Diamond) with orders of magnitude difference in thermal conductivity from $\sim 10^1$ to $\sim 10^3$. We found that critical D is almost the same for the different materials, implying that the model does not seem to be affected by the magnitude of the materials' thermophysical properties. In conclusion, for most metal-bulk material systems, choosing $D > 20$ guarantees both model capacity and low computational resources.

B. E effect of parameter bounds

We constructed a virtual Au coated SiC (Au-SiC) material for studying the effect of bounds on the model accuracy. The details of the virtual material information are given in Table I. With the TTR model, we created a large number of testing curves for virtual Au-SiC with different combinations of TBCs and TCs. We then used the DL model trained with $D = 100$ to output the TBC and TC of the testing curves. Figure 5(a) shows the predicted TC as a

function of input TC under different input TBCs. Notably, when TC approaches the bounds, the accuracy of prediction is affected. This is due to the small number of samples near the boundary in the training data, potentially hindering the model's ability to fully capture the characteristics of these parameters. Moreover, the predicting accuracy for TC is poorer when it is close to the lower bound than upper bound. The MSE loss function may focus more on the prediction of upper bounds, resulting in inferior performance of the model in the prediction of lower bounds. The input TBC also influences the predicting accuracy for TC. When the input TBC is at the lower (20 MW/m² K) or upper bound (300 MW/m² K), it has the most significant impact on TC predictions. However, this effect is pronounced (error $> 5\%$) only when TC is also near the lower bound. Figure 5(b) shows the predicted TBC as a function of input TBC under different TCs. The TBC prediction accuracy is affected by its bounds in a similar way as predicting TC. The reason for the poorer prediction accuracy when the TBC approaches the lower bound than the upper bound may be due to the higher sensitivity of the TBC, which requires more training data to capture the pertinent features for accurate prediction. The effect of the input TC on the prediction accuracy of the TBC is similar to the effect of the input TBC on the prediction accuracy of the TC as described previously. In summary, if both TC and TBC approach their bounds, DL models may encounter challenges in ensuring accurate predictions; Accurate predictions can be ensured if one of the parameters is avoided near the bounds, suggesting that maintaining larger bounds during training is advantageous.

C. Model validation with experimental results

1. Metal-bulk samples

Al-Sa and Au/Ti-SiC samples were fabricated for model validation. The Al-sapphire sample was measured by 785-TTR described in Sec. II, and the Au/Ti-SiC sample was measured by 532-TTR. Al and Au were coated on Sa and SiC by thermal evaporation. For the Au coating, 5 nm Ti was coated for the adhesion layer. Atomic force microscope (AFM) and profilometer were used to measure the metal layer thicknesses, with 100/5 and 80 nm

29 October 2024 18:18:32

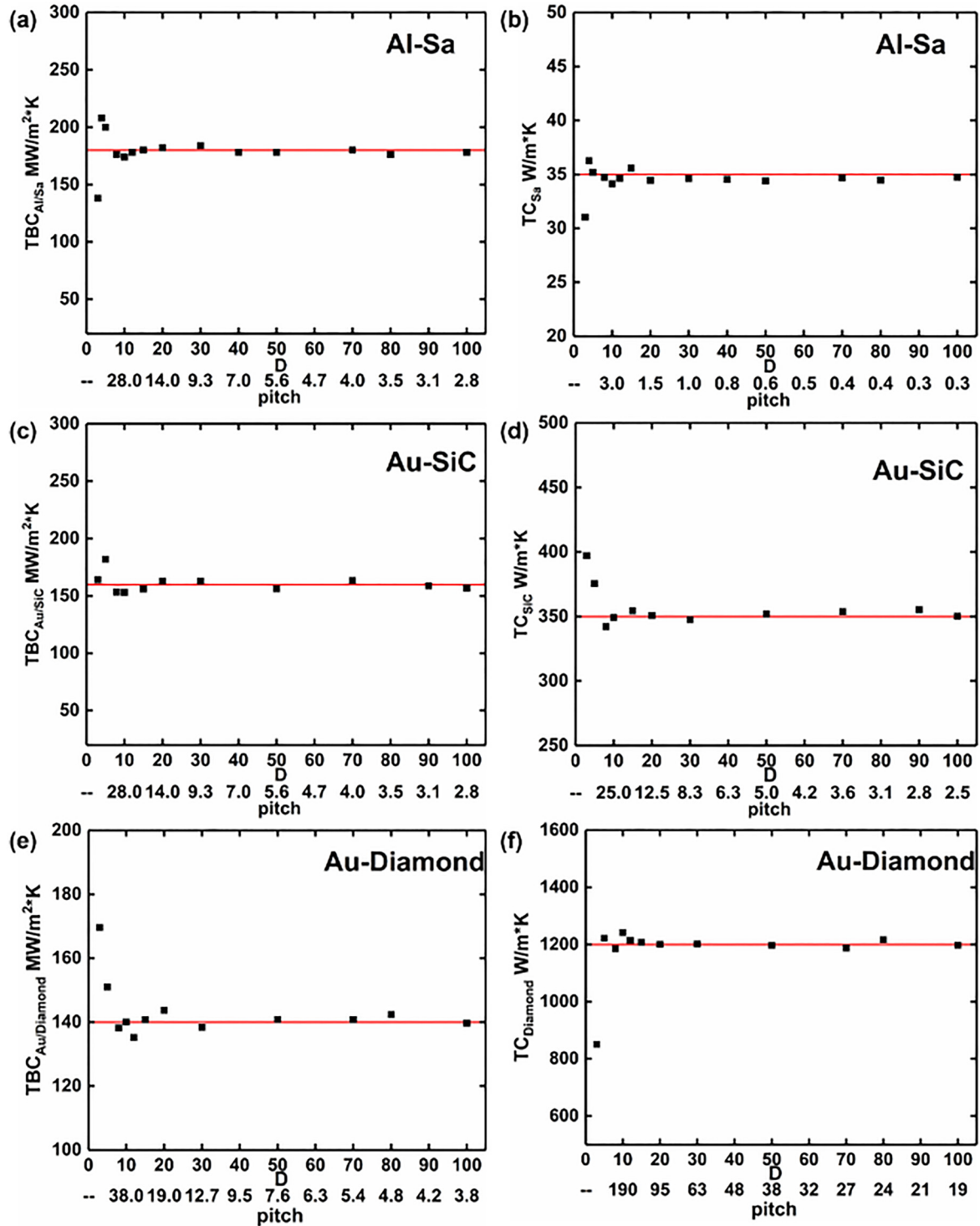


FIG. 4. DL model predictions at different training set densities (D) and pitch ($\frac{\text{upper bound} - \text{lower bound}}{D-1}$) for Al-Sa: (a) $TBC_{Al/Sa}$ and (b) TC_{Sa} ; DL model predictions at different training set densities (D) for Au-SiC: (c) $TBC_{Au/SiC}$ and (d) TC_{SiC} ; and DL model predictions at different training set densities (D) for Au-diamond: (e) $TBC_{Au/Diamond}$ and (f) $TC_{Diamond}$.

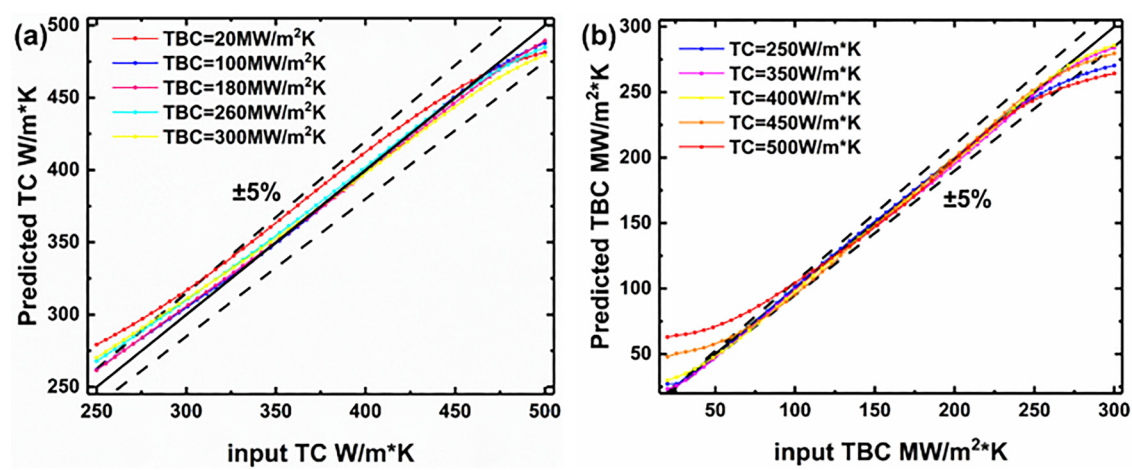


FIG. 5. Compare results of the DL model predicting (a) TC and (b) TBC.

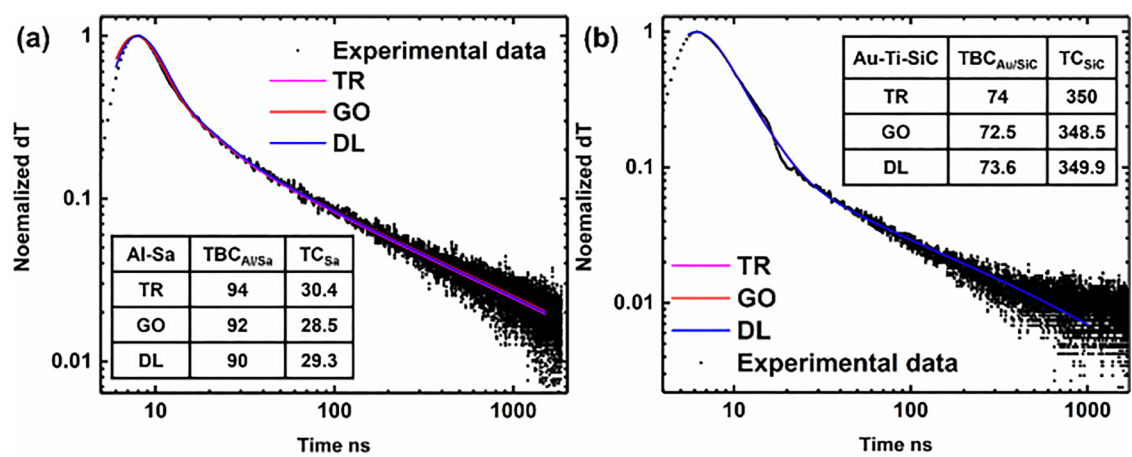


FIG. 6. (a) Measured transients against the model curves fitted by DL, Trust Region and Global Optimization for this Al-Sa sample. (b) Measured transients against the model curves fitted by DL, Trust Region and Global Optimization for this Au-Ti-SiC sample.

TABLE II. Material thickness, density, specific heat capacity, and thermal conductivity information at room temperature and unknown parameters' bounds and D range.

		Thickness (nm)	Density (kg/m ³)	Specific heat capacity (J/kg K)	Thermal conductivity (W/m K)	Lower bounds	Upper bounds	D range
GaN-on-SiC	UID-GaN	400	6 150 ⁵⁰	470 ⁵¹	Fit	50	250	2-50
	Fe-GaN	1 500		430 ⁵²	Fit	20	200	2-50
	TBC _{GaN/SiC} (MW/m ² K)			Fit		40	300	2-50
	SiC	1 000 000	3 260 ³¹	690 ²⁹	300 ²²
GaN-on-Si	UID-GaN	200	6 150 ⁵⁰	470 ⁵¹	Fit	50	250	2-50
	C-GaN	800		430 ⁵²	Fit	20	200	2-50
	AlGaN buffer	3 650			Fit	1	25	2-50
	Si	1 000 000	2 200 ³¹	700 ⁵³	140 ³⁸

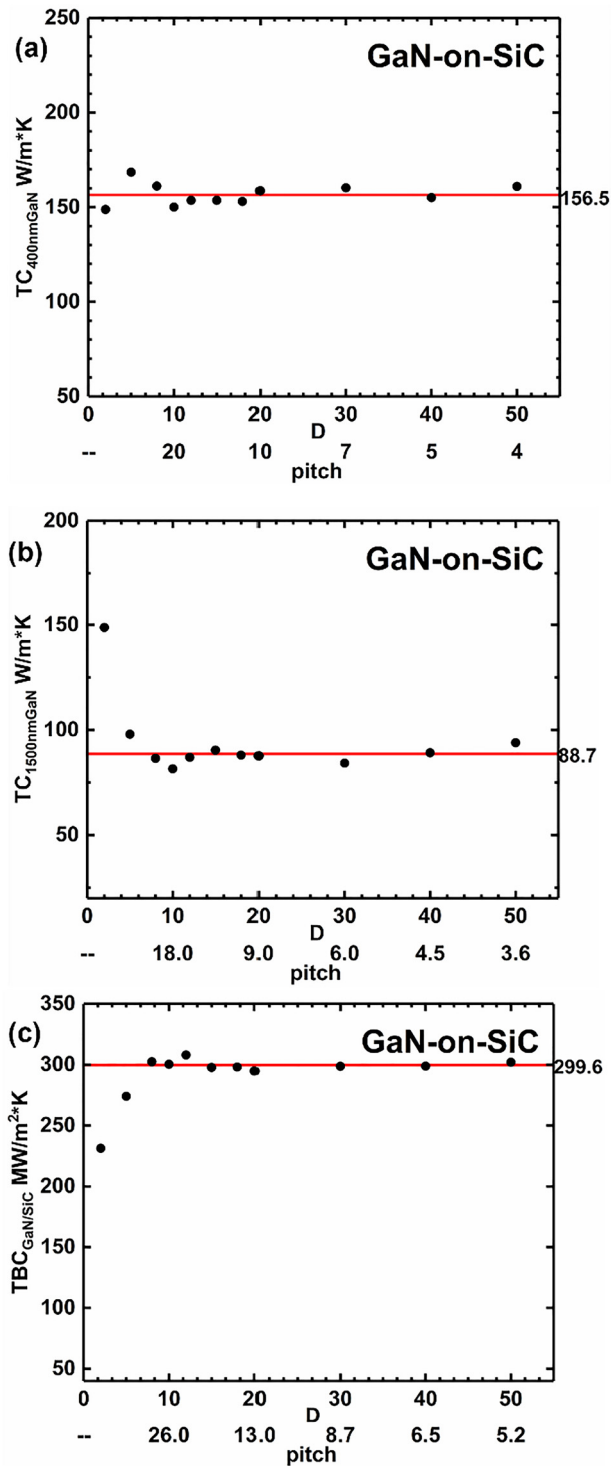


FIG. 7. DL model predictions at different training D and pitch ($\frac{\text{upper bound} - \text{lower bound}}{D - 1}$) for GaN-on-SiC: (a) $TC_{400nmGaN}$, (b) $TC_{1500nmGaN}$, and (c) $TBC_{GaN/SiC}$.

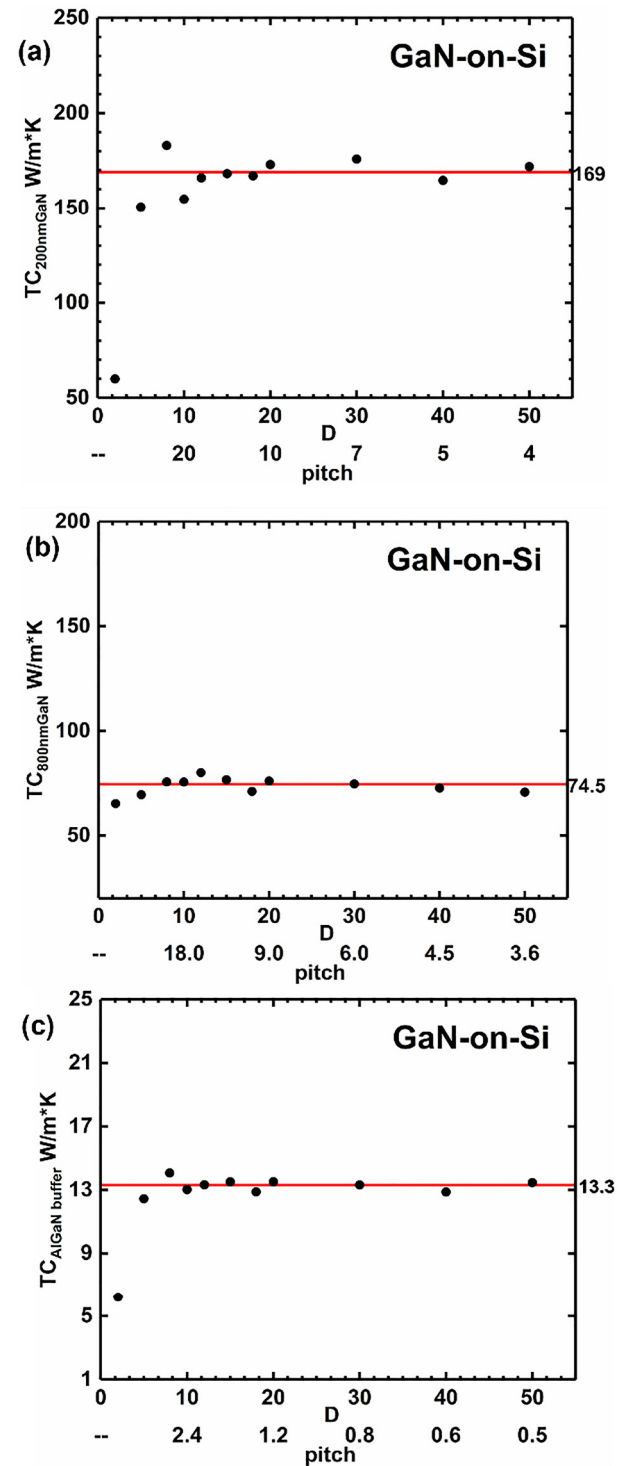


FIG. 8. DL model predictions at different training D and pitch ($\frac{\text{upper bound} - \text{lower bound}}{D - 1}$) for GaN-on-Si: (a) $TC_{200nmGaN}$, (b) $TC_{800nmGaN}$, and (c) $TC_{AlGaN \text{ buffer}}$.

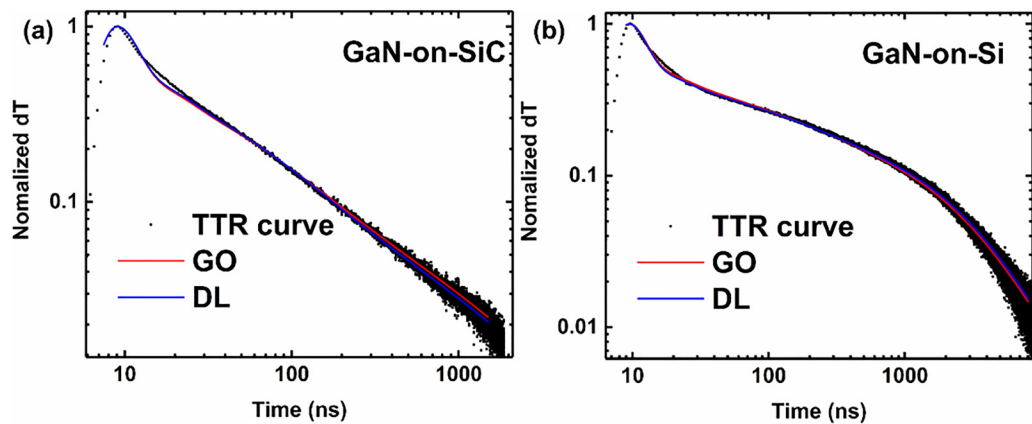


FIG. 9. The measured transients against the model curves fitted by DL and Global Optimization for (a) GaN-on-SiC and (b) GaN-on-Si.

determined for Au/Ti and Al, respectively. A four-probe technique was used to measure the thermal conductivities of metals, determined from the electrical resistivity by using the Wiedemann–Franz law. The other controlled properties of materials are given in Table I. The unknown parameters in Al-Sa and Au/Ti-SiC samples are the metal-bulk TBC and bulk thermal conductivity.

The measured TTR curve of the Al-sapphire sample was plotted in Fig. 6(a). The bounds used in the model were summarized in Table I and the D is 100. In Fig. 6(a), the DL fitting curve is overlaid with the measured TTR transient. For comparison, the traditional least-square fitting method (i.e., Global Optimization, Trust Region, and Levenberg Marquardt algorithms) is used to fit the same transient, with the fitted curve also plotted in Fig. 6(a). The figure shows that the four methods rendered the almost identical fitting curve. In addition, as shown in the table inset of Fig. 6(a), the TBC and TC predicted by the DL model are consistent with those by Global Optimization and Trust Region (the difference is less than $\pm 5\%$). It should be noted that the fitted results from Levenberg Marquardt are same to the results from the Trust Region. Therefore, only the results from Trust Region are plotted in Figs. 6(a) and 6(b). Figure 6(b) plotted the measured transients against the model curves fitted by DL, Global Optimization, and Trust Region for the Au/Ti-SiC sample. Table inset of Fig. 6(b) compared the fitted thermal properties' results between four methods. It was also shown that DL fitted results are consistent with results fitted by Global Optimization and Trust Region. Based on the bound study in Sec. IV B, we confirm that the predicted results are free from the bounds effects, validating the predicting accuracy.

2. GaN-on-SiC/Si samples

We discuss the implantation of the DL method on the multi-layer structure with more variables. The multilayer GaN-on-SiC and GaN-on-Si structures were studied in the presented work. The GaN-on-SiC structure consists of a ~ 25 nm AlGaIn layer, a 400 nm unintentional doping (UID)-GaIn layer, a 1500 nm Fe-doped GaIn layer, and an AlN nucleation layer on a 4H-SiC substrate. The GaN-on-Si layer structure consists of a 25 nm AlGaIn layer, a 200 nm unintentional doping (UID)-GaIn layer, an 800 nm C-doped GaIn layer, and a 3650 nm AlGaIn buffer layer on the Si substrate. The detailed information of GaN-on-SiC material was also given in Ref. 22. The two samples were measured by 320-TTR described in Sec. II. In Table II, all unknown parameters to be fitted are indicated. The top AlGaIn layers can be ignored in the fitting analysis.²² The information of D and bounds and all the other controlled parameters are also summarized in Table II. Figure 7(a)–7(c) show the DL predictions as a function of D for the $TC_{400\text{nmGaIn}}$, $TC_{1500\text{nmGaIn}}$, and $TBC_{\text{GaN/SiC}}$, respectively. $TC_{400\text{nmGaIn}}$ and $TC_{1500\text{nmGaIn}}$ stabilize when $D > 15$ with an error of no more than $\pm 5\%$. The trend of $TBC_{\text{GaN/SiC}}$ is similar to that of $TC_{400\text{nmGaIn}}$, tending to stabilize after $D > 15$ with an error range within $\pm 2\%$. Compared with the metal-bulk samples discussed in Sec. IV A, the D needed for the prediction convergence for this GaN-on-SiC sample is almost the same. For the GaN-on-Si sample, DL predictions for $TC_{200\text{nmGaIn}}$, $TC_{800\text{nmGaIn}}$, and $TC_{\text{AlGaIn buffer}}$ as a function of D are plotted in Figs. 8(a)–8(c). $TC_{200\text{nmGaIn}}$ and $TC_{800\text{nmGaIn}}$ show the similar trend, stabilizing with an error of no

29 October 2024 18:18:32

TABLE III. Summary of fitted data by GO and DL for the GaN-on-SiC and GaN-on-Si.

Materials		GaN-on-SiC			GaN-on-Si	
Properties	$TC_{\text{GaN}400\text{nm}}$	$TC_{\text{GaN}1500\text{nm}}$	$TBC_{\text{GaN/SiC}}$	$TC_{\text{GaN}200\text{nm}}$	$TC_{\text{GaN}800\text{nm}}$	$TC_{\text{AlGaIn buffer}}$
Unit	W/m K	W/m K	MW/m ² K	W/m K	W/m K	W/m K
GO	160	94	200	172	74	13.7
DL	157	89	300	169	74.5	13.3

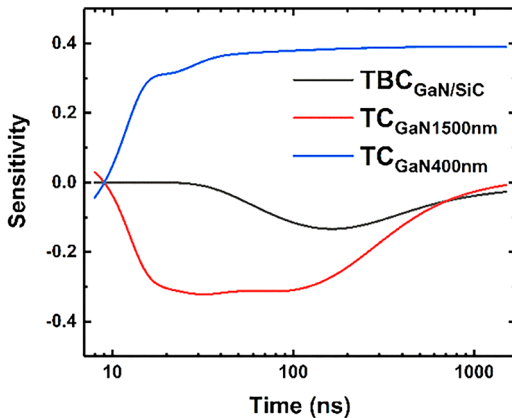


FIG. 10. Sensitivities of the signals in the TTR signal of $\text{TC}_{400\text{nmGa}}\text{N}$, $\text{TC}_{1500\text{nmGa}}\text{N}$, and $\text{TBC}_{\text{GaN/SiC}}$ of the GaN-on-SiC sample.

more than $\pm 5\%$ after $D > 12$. $\text{TC}_{\text{AlGa}}\text{N}$ buffer oscillates significantly at $D < 10$, whereas at $D > 10$, the $\text{TC}_{\text{AlGa}}\text{N}$ buffer stabilizes with an error of no more than $\pm 5\%$. By comparing the results of the two materials, it was found that although the thermal properties and the given bounds of the materials are of different magnitudes, the critical D is roughly the same. In this work, $D_1 = D_2 = \dots = D_X = D$, the size of the data set is equal to the D^X . As D increases, the size of the data set exponentially increases, making it take significantly increased time to generate the data set. In addition, it will take much more time for model iteration and hyperparameter updates. Since X in multilayer material is larger, controlling D to be a smaller value in the multilayer system is more important for computational costs, with respect to the bulk system. For the most of materials, controlling $D > 20$ can ensure both the accuracy of the predictions and low computational costs.

As shown in Figs. 9(a) and 9(b), the fitted curves by the DL model are consistent with those by the Global Optimization method. Table III summarized the fitted data for the GaN-on-SiC and GaN-on-Si materials. For the GaN-on-SiC, the $\text{TC}_{\text{GaN}400\text{nm}}$ and $\text{TC}_{\text{GaN}1500\text{nm}}$ predicted by the DL model are consistent with those by the Global Optimization method. The discrepancies of these two parameters are $< \pm 2\%$ and $\pm 5.4\%$, respectively. However, the discrepancy is larger in the fitted $\text{TBC}_{\text{GaN/SiC}}$. Figure 10 shows sensitivities of the TTR signal to $\text{TC}_{400\text{nmGa}}\text{N}$, $\text{TC}_{1500\text{nmGa}}\text{N}$, and $\text{TBC}_{\text{GaN/SiC}}$. Sensitivity analysis are commonly used in TTR measurement to quantitatively analyze the fitting capability, with more details introduced in Ref. 22. As shown in Fig. 10, the sensitivity to $\text{TBC}_{\text{GaN/SiC}}$ is much lower compare to the sensitivities to the other two parameters, resulting in a lower fitting accuracy with both DL and GO methods. Figure 9 indicates that the TTR signal has a smaller signal-to-noise ratio after 200 ns, which also affects the accuracy. For the GaN-on-Si, all the DL fitted results ($\text{TC}_{200\text{nmGa}}\text{N}$, $\text{TC}_{800\text{nmGa}}\text{N}$, and $\text{TC}_{\text{AlGa}}\text{N}$ buffer) are consistent with those fitted by Global Optimization, as shown in Table III.

Compared to traditional methods, well-built DL models take less calculation time. With the same computer configuration, it

takes only a few milliseconds to analyze a single experimental curve by the DL model, while traditional fitting methods such as GO take several minutes. Compared to the traditional fitting method that requires searching for the optimal solution for each data, deep learning models are data-driven, enabling faster inference and stronger fitting capabilities. Therefore, they are more efficient and effective in handling large-batch measurement applications with similar structures. Certainly, it is worth noting that the whole process of building the DL models takes some time. However, even considering the time involved, it remains efficient compared to traditional methods. In addition, this paper investigates the effect of the training set size (D) and bounds, providing ideas for efficiently and reliably building the model. The in-depth analysis further strengthens the application value of the DL model for massive data processing. Deep learning models also have limitations: First, it needs to build training sets and models for each object. In addition, it has been applied mainly on the bulk material system and thin film/substrate material system, the multilayer systems need to be further studied. The last but not the least, similar to the non-linear least squares fitting methods (the Global Optimization, Levenberg-Marquart, Trust Region, etc.) predicting parameters that are highly correlated or have low measurement sensitivity remains challenging.

V. CONCLUSION

In this work, deep learning models are built to process data from TTR experiments with high accuracy and efficiency. A reliable training set construction method is first defined by investigate the influence of density and bound. For both bulk materials and GaN-based epitaxial wafers, a training set density > 20 ensures the prediction performance of the deep learning model. We also find that the accuracy of the deep learning model tends to decrease when the predictions are close to the bounds of the unknown parameters. It is better to keep the bounds larger. More deeply, we can combine the prediction for each unknown parameter to determine whether the results are reliable or not. We confirmed the deep learning models using the samples with different structures and properties (bulk materials, thin film materials: GaN-based epitaxial wafers). For bulk materials, the predictions of the DL models were less than 3% different from the GO/RT fitting results based on the thermal model; and for GaN-based epitaxial wafers, the predictions of the parameters were consistent with the GO fitting results (difference $< 6\%$), except for $\text{TBC}_{\text{GaN/SiC}}$ DL predictions. $\text{TBC}_{\text{GaN/SiC}}$ DL prediction is poor because of the low sensitivity of this parameter in the thermal model, the overlap of the sensitivity with the $\text{TC}_{\text{GaN}1500\text{nm}}$ and the influence of the experimental noise. The traditional fitting method (\sim seconds) takes 1000 times longer than the DL method (\sim milliseconds) with the same computer configuration. In summary, we demonstrated that deep learning models have the ability to perform high-precision and rapid analysis in the TTR measurement of various material systems, making the TTR technology has the great potential to be used as a process monitoring tool in the semiconductor manufacturing line.

ACKNOWLEDGMENTS

The authors acknowledge financial support from the National Natural Science Foundation of China (NNSFC) under Grant

29 October 2024 18:18:32

No.62104173 and the Key Research and Development Program of Hubei Province under Grant No. 2021BAA055. The authors would like to express sincere appreciation to Mr. Han Wu for his invaluable contributions and support throughout this work.

AUTHOR DECLARATIONS

Conflict of Interest

The authors have no conflicts to disclose.

Ethics approval

No experiments on animal or human subjects were used for the preparation of the submitted manuscript.

Author Contributions

Yali Mao: Conceptualization (equal); Data curation (lead); Investigation (lead); Methodology (equal); Writing – original draft (equal). **Shaojie Zhou:** Investigation (equal); Methodology (equal). **Weiyuan Tang:** Methodology (equal). **Mei Wu:** Writing – review & editing (equal). **Haochen Zhang:** Writing – review & editing (equal). **Haiding Sun:** Writing – review & editing (equal). **Chao Yuan:** Conceptualization (lead); Funding acquisition (lead); Methodology (lead); Supervision (lead); Writing – original draft (equal); Writing – review & editing (lead).

DATA AVAILABILITY

The implemented codes of the DL model will be publicly available along with the data set associated with this study at Github, <https://github.com/ZZSJ402/DL-TTR>.

REFERENCES

- ¹D. G. Cahill, “Analysis of heat flow in layered structures for time-domain thermoreflectance,” *Rev. Sci. Instrum.* **75**(12), 5119–5122 (2004).
- ²J. Zhu, D. Tang, W. Wang, J. Liu, K. W. Holub, and R. Yang, “Ultrafast thermoreflectance techniques for measuring thermal conductivity and interface thermal conductance of thin films,” *J. Appl. Phys.* **108**(9), 094315 (2010).
- ³T. L. Bougher, L. Yates, C.-F. Lo, W. Johnson, S. Graham, and B. A. Cola, “Thermal boundary resistance in GaN films measured by time domain thermoreflectance with robust Monte Carlo uncertainty estimation,” *Nanoscale Microscale Thermophys. Eng.* **20**(1), 22–32 (2016).
- ⁴A. J. Schmidt, R. Cheaito, and M. Chiesa, “A frequency-domain thermoreflectance method for the characterization of thermal properties,” *Rev. Sci. Instrum.* **80**(9), 094901 (2009).
- ⁵A. J. Schmidt, R. Cheaito, and M. Chiesa, “Characterization of thin metal films via frequency-domain thermoreflectance,” *J. Appl. Phys.* **107**(2), 024908 (2010).
- ⁶B. Meng, Y. Ma, X. Wang, and C. Yuan, “Quantitative study on thermoreflectance linear relation,” *J. Appl. Phys.* **134**(11), 115102 (2023).
- ⁷C. Yuan, W. M. Waller, and M. Kuball, “Nanosecond transient thermoreflectance method for characterizing anisotropic thermal conductivity,” *Rev. Sci. Instrum.* **90**(11), 114903 (2019).
- ⁸J. Walachová, R. Zeipl, J. Zelinka, V. Malina, M. Pavelka, M. Jelínek, V. Studnička, and P. Lošťák, “High room-temperature figure of merit of thin layers prepared by laser ablation from Bi₂Te₃ target,” *Appl. Phys. Lett.* **87**(8), 081902 (2005).
- ⁹R. Garrelts, A. Marconnet, and X. Xu, “Assessment of thermal properties via nanosecond thermoreflectance method,” *Nanoscale Microscale Thermophys. Eng.* **19**(4), 245–257 (2015).
- ¹⁰J. Jeong, X. Meng, A. K. Rockwell, S. R. Bank, W.-P. Hsieh, J.-F. Lin, and Y. Wang, “Picosecond transient thermoreflectance for thermal conductivity characterization,” *Nanoscale Microscale Thermophys. Eng.* **23**(3), 211–221 (2019).
- ¹¹J. L. Braun, D. H. Olson, J. T. Gaskins, and P. E. Hopkins, “A steady-state thermoreflectance method to measure thermal conductivity,” *Rev. Sci. Instrum.* **90**(2), 024905 (2019).
- ¹²M. S. B. Hoque, Y. R. Koh, J. L. Braun, A. Mamun, Z. Liu, K. Huynh, M. E. Liao, K. Hussain, Z. Cheng, E. R. Hoglund, D. H. Olson, J. A. Tomko, K. Aryana, R. Galib, J. T. Gaskins, M. M. M. Elahi, Z. C. Leseman, J. M. Howe, T. Luo, S. Graham, M. S. Goorsky, A. Khan, and P. E. Hopkins, “High in-plane thermal conductivity of aluminum nitride thin films,” *ACS Nano* **15**(6), 9588–9599 (2021).
- ¹³X. Qian, P. Jiang, and R. Yang, “Anisotropic thermal conductivity of 4H and 6H silicon carbide measured using time-domain thermoreflectance,” *Mater. Today Phys.* **3**, 70–75 (2017).
- ¹⁴Z. Guo, A. Verma, X. Wu, F. Sun, A. Hickman, T. Masui, A. Kuramata, M. Higashiwaki, D. Jena, and T. Luo, “Anisotropic thermal conductivity in single crystal β -gallium oxide,” *Appl. Phys. Lett.* **106**(11), 111909 (2015).
- ¹⁵C. Yuan, J. Li, L. Lindsay, D. Cherns, J. W. Pomeroy, S. Liu, J. H. Edgar, and M. Kuball, “Modulating the thermal conductivity in hexagonal boron nitride via controlled boron isotope concentration,” *Commun. Phys.* **2**(1), 43 (2019).
- ¹⁶C. Yuan, R. Hanus, and S. Graham, “A review of thermoreflectance techniques for characterizing wide bandgap semiconductors’ thermal properties and devices’ temperatures,” *J. Appl. Phys.* **132**(22), 220701 (2022).
- ¹⁷S. B. Kotsiantis, I. D. Zaharakis, and P. E. Pintelas, “Machine learning: A review of classification and combining techniques,” *Artif. Intell. Rev.* **26**(3), 159–190 (2006).
- ¹⁸Y. Pang, P. Jiang, and R. Yang, “Machine learning-based data processing technique for time-domain thermoreflectance (TDTR) measurements,” *J. Appl. Phys.* **130**(8), 084901 (2021).
- ¹⁹W. Shen, D. Vaca, and S. Kumar, “Reconsidering uncertainty from frequency domain thermoreflectance measurement and novel data analysis by deep learning,” *Nanoscale Microscale Thermophys. Eng.* **24**(3–4), 138–149 (2020).
- ²⁰B. F. Donovan, C. J. Szejewski, J. C. Duda, R. Cheaito, J. T. Gaskins, C.-Y. Peter Yang, C. Constantin, R. E. Jones, and P. E. Hopkins, “Thermal boundary conductance across metal-gallium nitride interfaces from 80 to 450 K,” *Appl. Phys. Lett.* **105**(20), 203502 (2014).
- ²¹J. Cho, D. Francis, D. H. Altman, M. Asheghi, and K. E. Goodson, “Phonon conduction in GaN-diamond composite substrates,” *J. Appl. Phys.* **121**(5), 055105 (2017).
- ²²C. Yuan, B. Meng, Y. Mao, M. Wu, F. Jia, L. Yang, X. Ma, and Y. Hao, “Transducer-less thermoreflectance technique for measuring thermal properties of the buried buffer layer and interface in GaN-based HEMTs,” *ACS Appl. Electron. Mater.* **4**(12), 5984–5995 (2022).
- ²³C. Yuan, J. W. Pomeroy, and M. Kuball, “Above bandgap thermoreflectance for non-invasive thermal characterization of GaN-based wafers,” *Appl. Phys. Lett.* **113**(10), 102101 (2018).
- ²⁴W. Kohn and L. J. Sham, “Self-consistent equations including exchange and correlation effects,” *Phys. Rev.* **140**(4A), A1133–A1138 (1965).
- ²⁵J. P. Perdew, K. Burke, and M. Ernzerhof, “Generalized gradient approximation made simple,” *Phys. Rev. Lett.* **77**(18), 3865–3868 (1996).
- ²⁶J. Callaway, “Model for lattice thermal conductivity at low temperatures,” *Phys. Rev.* **113**(4), 1046–1051 (1959).
- ²⁷P. B. Allen, “Improved Callaway model for lattice thermal conductivity,” *Phys. Rev. B* **88**(14), 144302 (2013).
- ²⁸R. Landauer, “Spatial variation of currents and fields due to localized scatterers in metallic conduction,” *IBM J. Res. Develop.* **1**, 223 (1957).
- ²⁹W. A. Little, “The transport of heat between dissimilar solids at low temperatures,” *Can. J. Phys.* **37**(3), 334–349 (1959).
- ³⁰F. Pedregosa, G. Varoquaux, A. Gramfort, V. Michel, B. Thirion, O. Grisel, M. Blondel, P. Prettenhofer, R. Weiss, V. Dubourg, J. Vanderplas, A. Passos, D. Cournapeau, M. Brucher, M. Perrot, and E. Duchesnay, “Scikit-learn: Machine learning in python,” *J. Mach. Learn. Res.* **12**, 2825–2830 (2011).

- ³¹W. M. Haynes, *CRC Handbook of Chemistry and Physics*, 97th ed. (CRC Press, Boca Raton, 2016).
- ³²Y. Takahashi and H. Akiyama, "Heat capacity of gold from 80 to 1000 K," *Thermochim. Acta* **109**(1), 105–109 (1986).
- ³³I. L. Ferreira, "On the heat capacity of pure elements and phases," *Mater. Res.* **24**, e20200529 (2021).
- ³⁴D. C. Harris, *Materials for Infrared Windows and Domes: Properties and Performance* (SPIE, 1999).
- ³⁵D. A. Ditmars, S. Ishihara, S. S. Chang, G. Bernstein, and E. D. West, "Enthalpy and heat-capacity standard reference material: Synthetic sapphire (α -Al₂O₃) from 10 to 2250 K," *J. Res. Natl. Bur. Stan.* **87**(2), 159 (1982).
- ³⁶M. E. Levinstein, S. L. Rumyantsev, and M. S. Shur, *Properties of Advanced Semiconductor Materials: GaN, AlN, InN, BN, SiC, SiGe* (Academic Press, 2001).
- ³⁷Y. Wang, B. Zhou, G. Ma, J. Zhi, C. Yuan, H. Sun, Y. Ma, J. Gao, Y. Wang, and S. Yu, "Effect of bias-enhanced nucleation on the microstructure and thermal boundary resistance of GaN/SiNx/diamond multilayer composites," *Mater. Charact.* **201**, 112985 (2023).
- ³⁸Y. Wang, Z. Lu, A. K. Roy, and X. Ruan, "Effect of interlayer on interfacial thermal transport and hot electron cooling in metal-dielectric systems: An electron-phonon coupling perspective," *J. Appl. Phys.* **119**(6), 065103 (2016).
- ³⁹D.-W. Oh, S. Kim, J. A. Rogers, D. G. Cahill, and S. Sinha, "Interfacial thermal conductance of transfer-printed metal films," *Adv. Mater.* **23**(43), 5028–5033 (2011).
- ⁴⁰M. Blank and L. Weber, "Influence of the thickness of a nanometric copper interlayer on Au/dielectric thermal boundary conductance," *J. Appl. Phys.* **124**(10), 105304 (2018).
- ⁴¹S. M. Oommen, L. Fallarino, J. Heinze, O. Hellwig, and S. Pisana, "Role of vibrational properties and electron-phonon coupling on thermal transport across metal-dielectric interfaces with ultrathin metallic interlayers," *J. Phys.: Condens. Matter* **34**(46), 465701 (2022).
- ⁴²A. Manoi, J. W. Pomeroy, N. Killat, and M. Kuball, "Benchmarking of thermal boundary resistance in AlGaIn/GaN HEMTs on SiC substrates: Implications of the nucleation layer microstructure," *IEEE Electron Device Lett.* **31**(12), 1395–1397 (2010).
- ⁴³F. Mu, Z. Cheng, J. Shi, S. Shin, B. Xu, J. Shiomi, S. Graham, and T. Suga, "High thermal boundary conductance across bonded heterogeneous GaN–SiC interfaces," *ACS Appl. Mater. Interfaces* **11**(36), 33428–33434 (2019).
- ⁴⁴J. Kuzmík, S. Bychikhin, D. Pogany, C. Gaquière, E. Pichonat, and E. Morvan, "Investigation of the thermal boundary resistance at the III-nitride/substrate interface using optical methods," *J. Appl. Phys.* **101**(5), 054508 (2007).
- ⁴⁵J. Cho, E. Bozorg-Grayeli, D. H. Altman, M. Asheghi, and K. E. Goodson, "Low thermal resistances at GaN–SiC interfaces for HEMT technology," *IEEE Electron. Device Lett.* **33**(3), 378–380 (2012).
- ⁴⁶J. Cho, Y. Li, W. E. Hoke, D. H. Altman, M. Asheghi, and K. E. Goodson, "Phonon scattering in strained transition layers for GaN heteroepitaxy," *Phys. Rev. B* **89**(11), 115301 (2014).
- ⁴⁷J. Cho, Y. Li, D. H. Altman, W. E. Hoke, M. Asheghi, and K. E. Goodson, in *2012 IEEE Compound Semiconductor Integrated Circuit Symposium (CSICS)* (IEEE, La Jolla, CA, 2012), pp. 1–4.
- ⁴⁸A. Sarua, H. Ji, K. P. Hilton, D. J. Wallis, M. J. Uren, T. Martin, and M. Kuball, "Thermal boundary resistance between GaN and substrate in AlGaIn/GaN electronic devices," *IEEE Trans. Electron Devices* **54**(12), 3152–3158 (2007).
- ⁴⁹E. Ziade, J. Yang, G. Brummer, D. Nothorn, T. Moustakas, and A. J. Schmidt, "Thermal transport through GaN–SiC interfaces from 300 to 600 K," *Appl. Phys. Lett.* **107**(9), 091605 (2015).
- ⁵⁰H. Harima, "Properties of GaN and related compounds studied by means of Raman scattering," *J. Phys.: Condens. Matter* **14**(38), R967–R993 (2002).
- ⁵¹K. T. Jacob, S. Singh, and Y. Waseda, "Refinement of thermodynamic data on GaN," *J. Mater. Res.* **22**(12), 3475–3483 (2007).
- ⁵²B. A. Danilchenko, T. Paszkiewicz, S. Wolski, A. Jeżowski, and T. Plackowski, "Heat capacity and phonon mean free path of wurtzite GaN," *Appl. Phys. Lett.* **89**(6), 061901 (2006).
- ⁵³H. R. Shanks, P. D. Maycock, P. H. Sidles, and G. C. Danielson, "Thermal conductivity of silicon from 300 to 1400 K," *Phys. Rev.* **130**(5), 1743–1748 (1963).